A Numerical Study of Hurricane Erin (2001). Part II: Shear and the Organization of Eyewall Vertical Motion

Scott A. Braun* and Liguang Wu#

*Laboratory for Atmospheres, NASA/Goddard Space Flight Center, Greenbelt, MD

#Goddard Earth Science and Technology Center, University of Maryland, Baltimore County, Baltimore, MD

Submitted to

Monthly Weather Review

January 3, 2006

Corresponding Author: Dr. Scott Braun, Mesoscale Atmospheric Processes Branch, NASA/GSFC, Code 613.1, Greenbelt, MD 20771. Scott.A.Braun@nasa.gov.

Abstract

A high-resolution numerical simulation of Hurricane Erin (2001) is used to examine the organization of vertical motion in the eyewall and how that organization responds to a large and rapid increase in the environmental vertical wind shear and subsequent decrease in shear. During the early intensification period, prior to the onset of significant shear, the upward motion in the eyewall was concentrated in small-scale convective updrafts that formed in association with regions of concentrated vorticity (herein termed mesovortices) with no preferred formation region in the eyewall. Asymmetric flow within the eye was weak. As the shear increased, an azimuthal wavenumber 1 asymmetry in storm structure developed with updrafts tending to form on the downshear to downshear-left side of the eyewall. Continued intensification of the shear led to increasing wavenumber 1 asymmetry, large vortex tilt, and a change in eyewall structure and vertical motion organization. During this time, the eyewall structure was dominated by a vortex couplet with a cyclonic (anticyclonic) vortex on the downtilt-left (downtilt-right) side of the eyewall and strong asymmetric flow across the eye that led to strong mixing of eyewall vorticity into the eye. Upward motion was concentrated over an azimuthally broader region on the downtilt side of the eyewall, upstream of the cyclonic vortex, where low-level environmental inflow converged with the asymmetric outflow from the eye. As the shear diminished, the vortex tilt and wavenumber 1 asymmetry decreased, while the organization of updrafts trended back toward that seen during the weak shear period.

1. Introduction

The National Aeronautics and Space Administration (NASA) Tropical Rainfall Measuring Mission (TRMM) satellite has proven to be a valuable tool for the study of precipitation in hurricanes. Lonfat et al. (2004) used rainfall estimates from the TRMM Microwave Imager (TMI) to examine the climatological rainfall characteristics of hurricanes with emphases on the variations with respect to storm intensity and location (different ocean basins) and on asymmetries in rainfall structure. Cecil et al. (2002) and Cecil and Zipser (2002) examined TRMM radar, TMI, and lightning data in hurricanes and found that the precipitation characteristics were very similar to non-hurricane tropical oceanic precipitation. The hurricane outer rainbands produced more lightning per unit area than the eyewall and inner rainbands of hurricanes as well as other tropical oceanic convection and were proposed to be a preferred region for the presence of supercooled liquid water. Kelley et al. (2004, 2005) described the occurrence of tall convective towers in the eyewall and found that the chance of intensification increases when such towers are present. Pu et al. (2002) compared mesoscale simulations of Supertyphoon Paka (1997) initialized with global analyses that either included or excluded TRMM rainfall information and found that the assimilation of the rainfall data significantly improved the simulated intensity and kinematic and precipitation structures of the storm. Braun (2006) used TRMM radar reflectivity data for validation of a numerical simulation of Hurricane Bonnie (1998) and showed that the model significantly overproduced precipitation, in part because of water conservation errors associated with the model numerics.

Key to understanding the precipitation distribution in hurricanes is an understanding of factors determining the distribution of vertical motion. While the tangential wind field is dominated by its azimuthal mean component (Fig. 1a), which is more than an order of magnitude larger than its higher wavenumber components, the vertical motion field is comprised of large contributions from its higher wavenumber components (Fig. 1b). For the case to be examined in this study, the amplitudes of vertical motion associated with wavenumber 1 and wavenumbers 4 and higher are actually larger than the azimuthal mean component for most of the simulation.

Significant wavenumber 1 contributions to vertical motion frequently derive from the effects of storm motion and vertical wind shear[1]. Shapiro (1983), using a slab boundary layer model, showed that a translating storm develops asymmetries in the pattern of frictional convergence within the boundary layer such that the maximum convergence, and implied low-level upward motion, occurs in front of the storm. Several mechanisms have been proposed by which vertical shear, in the environment or from beta gyres, produces wavenumber 1 asymmetries in vertical motions. Readers are referred to much more in-depth summaries in Jones (1995), Wang and Holland (1996), Bender (1997), Frank and Ritchie (1999, 2001), Corbosiero and Molinari (2002), and Reasor et al. (2004). Briefly, the studies can be summarized as follows:

- In adiabatic vortices, the vertical motion asymmetry is related to vortex tilt and its associated temperature perturbations. Initially, upward motion occurs in the downtilt direction, but subsequently shifts to the right of the tilt direction as the mean vortex flow moves along the sloped isentropes associated with the vortex tilt (Jones 1995, Wang and Holland 1996, Frank and Ritchie 1999).

---

[1] Other contributions can be associated with beta gyres (Wang and Holland 1996, Bender 1997) and air-sea interaction (Wu et al. 2005)

- In diabatic vortices, upward motion occurs in the downshear direction or somewhat to the left of the shear vector, while precipitation occurs downshear left (Wang and Holland 1996; Frank and Ritchie 1999, 2001). While asymmetries can occur in the absence of significant vortex tilt (Reasor et al. 2000), when significant tilt exists, the upward vertical motion is frequently aligned in the tilt direction (Rogers et al. 2003, Braun et al. 2006, Wu et al. 2006).
- Both real-case and idealized studies have found a consistent relationship between the storm-relative asymmetric flow and the eyewall vertical motion asymmetries (Bender 1997; Frank and Ritchie 1999, 2001; Braun et al. 2006; Wu et al. 2006). Where the relative flow is directed inward (outward) in the eyewall, the negative (positive) vorticity advection is approximately balanced by vortex stretching (shrinking) associated with convergence (divergence). For a vortex in unidirectional shear, low-level inflow and upper-level outflow occur on the downshear side of the vortex, thereby producing low-level convergence and upper-level divergence and a deep layer of upward vertical motion. The opposite occurs on the upshear side of the vortex.

The contribution to vertical motion from wavenumbers 4 and higher is generally associated with convective features in the eyewall. Both observations and modeling show that convective updrafts occupy only a small percentage of the eyewall area, but contribute a major portion of the vertical mass flux (Riehl and Malkus 1961, Jorgensen et al. 1985, Black et al. 1996, Braun 2002, Eastin et al. 2005). Braun (2006), using a high-resolution simulation of Hurricane Bonnie (1998), found that about 75% (50%) of the eyewall condensation occurred in updrafts stronger than 2 m s^{-1} (4 m s^{-1}), indicating the important role of convective towers in eyewall precipitation production. Black et al. (2002) described the structure of eastern Pacific hurricanes Jimena (1991) and Olivia (1994) using aircraft radar and flight-level in-situ data. In both cases, shear produced a wavenumber-1 distribution of convection with the highest reflectivities in the semicircle to the left of the shear direction. The convective cells comprising this reflectivity asymmetry were periodic, with echoes forming on the downshear side of the eyewall, growing and maturing on the left side of the shear vector, and often dissipating on the upshear side. In some cases, clusters of cells were observed to move around the eyewall multiple times, initiating new bursts of convection as they moved again into the downshear portion of the eyewall. Braun et al. (2006) described a similar behavior of convective updrafts in their simulation of Hurricane Bonnie (1998). They showed that, in that simulation, the updrafts were typically associated with relatively long-lived eyewall mesovortices that moved around the eyewall. As the mesovortices moved into the downshear side of the eyewall, updrafts often formed where the cyclonic outflow associated with the mesovortices encountered the low-level relative inflow associated with the vertical wind shear. The updrafts dissipated when the mesovortices subsequently moved into the upshear side of the eyewall. In some examples, the mesovortices continued around the eyewall and later initiated subsequent episodes of convection upon re-entering the downshear side of the eyewall.

The purpose of this study is to examine the organization of vertical motion in Hurricane Erin (2001) and compare the results to those for Hurricane Bonnie (1998) described by Braun et al. (2006). Wu et al. (2006) described the simulation of Erin, including validation against available observations, and examined the role of vertical shear in the overall evolution of the storm. Here, we specifically focus on the impacts of shear on the organization of vertical motion and determine what role eyewall mesovortices play in this organization. Section 2 provides a summary of the numerical model configuration, physics options, and initial conditions. Section 3 provides a description of the simulated intensity and evolution and their relationship to changes in vertical wind shear while section 4 examines the organization of vertical motion. A brief comparison to the simulation of Hurricane Bonnie is provided in section 5 and conclusions are given in section 6.

2. Simulation description

The simulation examined in this study is similar to that used by Wu et al. (2006), but is extended to higher horizontal grid resolution to facilitate the study of more well-resolved updraft structures. The model used is the Pennsylvania State University-National Center for Atmospheric Research (PSU-NCAR) non-hydrostatic fifth generation mesoscale model (MM5 V3.4, Dudhia 1993, Grell et al. 1995). The original simulation of Wu et al. (2006) used three grids with grid spacings of 36, 12, and 4 km. The 36-km mother domain (Fig. 2) had 145×175 grid points in the x and y directions, respectively, and 27 vertical levels. An inner mesh with 12-km horizontal grid spacing consisted of 196×175 grid points while the 4-km nest had 151×151 grid points. The simulation was started at 0000 UTC 7 September 2001 and run for 96 hours, with model output saved every hour. Physics options for this simulation included a modified version of the Blackadar planetary boundary layer scheme (Blackadar 1979, Zhang and Anthes 1982) in which surface roughness calculations for momentum, temperature, and moisture follow Garratt (1992) and Pagowski and Moore (2001). Cloud processes were represented by the Betts-Miller cumulus parameterization scheme (Betts 1986; Betts and Miller 1986, 1993; Janjic 1994) on the 36- and 12-km grids and the Goddard Cumulus Ensemble model cloud microphysics (Tao and Simpson 1993, McCumber et al. 1991) on all grids. Radiative processes were represented by the cloudradiation scheme of Dudhia (1989).

The initial and boundary conditions for the 36-km domain were obtained from 12-hourly National Centers for Environmental Prediction (NCEP) surface and upper-air global reanalysis data sets. The sea-surface temperature (SST) data were derived from the NCEP SST analysis. The analysis fields, including temperature, geopotential height, winds, and relative humidity at mandatory pressure levels and with horizontal resolution of 2.5°×2.5° were interpolated horizontally to model grid points and vertically to the model vertical σ levels. No special observations were available near the initial time and no bogus vortex was included due to the weak and highly asymmetric structure of the observed system. The initial conditions for the nested 12-km domain were obtained by interpolating fields from the 36-km domain.

With 4-km grid spacing, deep convection is still poorly resolved. Some improvement of the convective structure can be obtained by reducing the grid spacing to 2 km. Because of computational limitations (limitation of moving grids to the inner-most mesh, available computer memory and computation time), a new simulation was conducted by using the original simulation to drive the initial and boundary conditions, via a one-way nesting procedure, for higher resolution grids. The new simulation was conducted by using 1-h output from the 12-km grid of the original simulation to provide initial and boundary conditions for a 6-km grid (337×253×27 grid points, Fig. 2) and 2-km grid (250×250×27) starting 24 h into the forecast to allow for some model spin up on the 12-km grid. The high-resolution grids were run for 72 hours until 0000 UTC 11 September. The 2-km grid was moved hourly to keep it centered on the storm. Model physics were identical to the original simulation except that no cumulus parameterization scheme was used and model output was saved every 30 minutes.

For most applications, including computation of storm motion and compositing of output fields to a storm-relative grid, the storm center was determined, as in Braun (2002), at every model output time using the pressure field at the lowest model level. The horizontal distribution of pressure was used to determine an approximate geometric center, or centroid, of the pressure field. The location of the minimum pressure was used as a first guess for the center. A variational approach was then used that adjusted the location of the center until the azimuthal variance of the pressure field at all radii between the center and the outer portion of the eyewall (~ 100 km) was minimized. This methodology worked well not only for identifying the centroid of the pressure field but also the approximate centroid of the ring of strong tangential winds and vorticity. Storm motion was then computed from the identified center locations. To compute the time-averaged fields shown in section 3, model output fields at all heights were transferred to a grid in which the storm's surface center was fixed with respect to time.

3. Simulated intensity, structure, and relation to shear

The change in horizontal grid spacing from 4 km in Wu et al. (2006) to 2 km in the present study produces relatively minor impacts on the simulated storm intensity and evolution. For a detailed description of the storm evolution and verification against data from the Fourth NASA Convection and Moisture Experiment (CAMEX-4) field program, see Wu et al. (2006). Here, we focus on specific aspects of the storm's evolution and its relationship to the environmental vertical wind shear. Many different measures of the vertical wind shear can be devised. Some studies use averages over regions within a few hundred (or less) kilometers of the center (Marks et al. 1992, Black et al. 2002, Rogers et al 2003), while others use averages over larger areas (Corbosiero and Molinari 2002, Zhu et al. 2004) or for large annuli that exclude much of the storm, e.g., averages over radii from 200-800 km (Kaplan and DeMaria 2003, Braun et al. 2006).

In the present study, an average over the innermost 300 km from the center is adopted and is found to provide a good measure of the near-core environmental shear. Use of data at larger radii incorporates larger-scale wind structures that are not immediately impacting the storm core and somewhat obscure the shear-intensity-structure relationships.

One notable difference between the original 4-km simulation and the newer 2-km simulation is seen in the time series of minimum seal-level pressure. In the 4-km simulation (Fig. 2a of Wu et al., 2006), the minimum sea-level pressure decreased throughout the simulation period, even after the onset of strong shear. In the 2-km simulation (Fig. 3a), the minimum sea-level pressure decreases rapidly until the onset of strong shear near 60 h (valid 1200 UTC September 9), remains steady or rises slightly for about 16 h, and then decreases further with the weakening of the shear. In contrast, the maximum surface winds are very similar between the two simulations, showing intensification until about 60 h followed by a period of relatively steady or slightly weakening winds. Wu et al. (2006), based upon studies by Schubert et al. (1999) and Kossin and Schubert (2001), argued that the steady decrease in minimum sea-level pressure and simultaneous decrease in the maximum winds seen in the 4-km simulation was a by-product of mixing of eyewall momentum into the eye. The different behavior of the minimum sea-level pressure in the 2-km simulation suggests that the change in horizontal resolution perhaps modifies that mixing of momentum.

The evolving shear impacts the precipitation and vertical motion fields during the course of Erin's lifecycle. Early on, when the shear is weak, the storm's precipitation is relatively symmetric and the vertical motion is relatively weak (Figs. 4a and 5a). Shortly after the shear begins to increase, vertical motions begin to increase and the upward motion part of a wavenumber 1 asymmetry becomes apparent on the northeastern side of the storm (Fig. 5b).

Reflectivities also increase (Fig. 4b) and become more asymmetric, with the maximum reflectivities slightly downstream of the upward motion. When the shear is strong (Figs. 4c-4e and 5c-5e), both the precipitation and vertical motion are highly asymmetric. Precipitation is found predominantly on just one side of the storm, with precipitation-free portions of the eyewall evident at 72 and 84 h (Figs. 4d and 4e). The outer precipitation region shifts from the northeastern side at 60 h (Fig. 4c) to the western side by 84 h (Fig. 4e), consistent with shifts seen in TRMM microwave imager data (see Wu et al. 2006). The upward motion is most intense during this period of strong shear (Figs. 5c-5e) and an adjacent region of strong downward motion is seen just downstream (in a cyclonic sense) from the updraft. This distribution is similar to observed storms under the influence of shear (Marks et al. 1992, Franklin et al. 1993, Black et al. 2002). As the shear weakens, the vertical velocity asymmetry outside the eyewall begins to decrease and the reflectivities become more symmetric as the outer precipitation redevelops and sweeps around the southern and eastern sides of the storm.

4. Organization of vertical motion

Our intent here is to examine the organization of vertical motion in the eyewall and compare the results from the simulation of Erin to those of Braun et al. (2006) for Hurricane Bonnie. In their analysis, Braun et al. (2006) used layer-averaged values to examine relationships between vorticity, vertical velocity, and asymmetric horizontal flow velocities. They chose a 3-km deep layer (from 1-4 km) just above the boundary layer because they wanted to highlight the deeper low-level structures, but avoid the effects of a shift in the mean wind direction across the top of the boundary layer that obscured the features of interest. In the present case, there is no comparable problem and features are best represented by layer averages between the surface and

3 km. Plots for three representative times are shown in Fig. 6 corresponding to periods with weak shear (<5 m s^{-1} between 850-200 mb, Fig. 6a), strong shear (> 5 m s^{-1}, Fig. 6b), and the return to weaker shear near the end of the simulation (Fig. 6c).

For the weak shear period (Fig. 7a), the eyewall frequently contains several areas of concentrated vorticity, some possessing closed circulations in the asymmetric flow field. We define these features as eyewall mesovortices. They form as a result of the vorticity dynamics of the eyewall. Specifically, an axisymmetric annulus of potential vorticity, representative of the distribution of vorticity within the eyewall of a hurricane, satisfies the Charney-Stern condition for inflection-point (mixed barotropic/baroclinic) instability (Montgomery and Shapiro 1995, Ren 1999, Nolan and Montgomery 2002). In the case of an unstable basic state, small perturbations grow rapidly to form polygonal eyewalls and mesovortices. Most of the mesovortices in the simulation also have attendant updrafts of varying magnitude, in some cases collocated with the mesovortex, in others somewhat trailing the mesovortex where outflow from the eye occurs as part of the mesovortex circulation. The movement of these relatively long-lived features cyclonically around the eyewall is apparent in the Hovmoller diagrams of vorticity and vertical motion in Fig. 7, although they are somewhat obscured by the strobe effect caused by the 30-min output frequency. The asymmetric flow within the eye is generally weak. As the shear increases, but is not too strong, the updrafts tend to shift to the downshear side of the eyewall where low-level asymmetric inflow is found (not shown). This relationship between updrafts and mesovortices is very similar to that seen in the Bonnie simulation of Braun et al. (2006).

When the shear exceeds 5 m s^{-1} after 48 h (00 UTC 9 September), a fairly rapid transition occurs to a highly asymmetric state with a pronounced wavenumber 1 asymmetry, as seen in Fig. 7. Initially, after the onset of this stronger shear, the upward motion is concentrated on the eastern side of the eyewall (Fig. 7b), but gradually shifts to the northern side of the eyewall by 60 h and the northwestern side by ~75 h. By 59 h (Fig. 6b), the low-level structure is characterized by an azimuthally broad region of upward motion on the northern side of the eyewall, slightly trailing (clockwise from) a region of concentrated cyclonic vorticity in the eyewall, with very weak vorticity on the eastern side. The combined wavenumbers 1 and 2 asymmetric fields (Fig. 6d) show pressure perturbations and circulations associated with a cyclonic/anticyclonic vortex couplet in the eyewall, strong flow across the eye from south to north, and relatively strong northeasterly flow outside the eyewall. The asymmetric flow across the eye appears to feed into the eyewall updrafts and may therefore be providing high θ_e air to the eyewall (Persing and Montgomery 2003, Cram e al. 2006) to enable the strong convection seen during this period (Fig. 5). Braun et al. (2006) and Cram et al. (2006) suggested that, in the case of their Bonnie simulations, the eyewall acted as a sort of containment vessel with little mean asymmetric flow across the eyewall and within the eye. The Erin simulation indicates that when the shear-induced wavenumber 1 asymmetry becomes sufficiently large, significant low-level ventilation of the eye occurs. Notice that the vorticity has increased significantly within the eye (Fig. 6b), suggestive of strong vorticity mixing from the eyewall to the eye (Schubert et al. 1999, Kossin and Eastin 2001, Kossin and Schubert 2001).

When the shear drops below 5 m s^{-1} near the end of the simulation (~90 h, Fig. 3), the wavenumber 1 asymmetry becomes much weaker (Fig. 7b). The low-level structure at 96 h (Fig. 6c) shows an annulus of vorticity, with various local maxima occurring around the eyewall, suggesting a trend back toward having mesovortices and their attendant updrafts within the eyewall. The asymmetric flow within the eye is weakening by this time.

The transitions from the mesovortex-dominated structure (Fig. 6a) to the vortex couplet and strong wavenumber 1 asymmetry (Figs. 5c-e and 6b) and back to a mesovortex structure (Fig. 6c) correspond closely to the onset and decline of strong vertical wind shear (cf. Figs. 3 and 7). The shear also causes a large tilt of the vortex to develop. Figure 8 shows the estimated 1-h average[2] displacements of the vortex centers at 5.9 and 9.3 km above mean sea level from the surface center location. The centers at these heights were estimated using the same method as for the surface center. However, at 9.3 km, during the period of strongest shear, this method was less effective, so the center was adjusted subjectively based upon the pressure pattern, wind speed, and wind vectors, with an emphasis on the circulation center, which was generally readily detectable. Displacements are only shown for the period following 36 h since the storm was still organizing before this time and the 9.3-km center position was much more variable. At 42 h (18 UTC 8 September), just prior to the onset of strengthening vertical wind shear, the vortex tilt is very small. As the southwesterly shear increases, the vortex tilt shifts to the northeast of the surface center (downshear) and increases in magnitude to about 10 km at 5.9 km and 18 km at 9.3 km by 54 h (06 UTC 9 September). By 72 h (00 UTC 10 September), near the time of peak shear, the vortex tilt is to the north-northwest (~55° to the left of the shear vector) and has reached a maximum magnitude of about 18 km at 5.9 km and 43 km at 9.3 km. As the shear decreases rapidly after 69 h, the vortex tilt also decreases rapidly, with the vortex essentially realigning by the end of the simulation. During the period in which there is appreciable tilt (~48-90 h), the strongest upward motion is always located in the general direction of the vortex tilt

---

[2] We use a three-point average of the center positions using data at a given time as well as at plus/minus one-half hour (the model output frequency).

(not shown). This relationship between vortex tilt and eyewall upward motion was noted previously for Hurricane Erin by Wu et al (2006) and for Hurricane Bonnie by Rogers et al. (2003) and Braun et al. (2006).

The vertical structure of the storm at the time of peak tilt is shown in Fig. 9 in a cross section oriented through the center in the direction of vortex tilt. The large tilt of the vortex is clearly evident from the isotachs of tangential velocity in the eyewall (Fig. 9a). Precipitation is found over a widespread area on the north (downtilt) side and is absent on the south (uptilt) side (cf. Fig. 4d). The perturbation potential temperature (Fig. 9b), derived as in Wu et al. (2006) using a composite reference sounding from Halverson et al. (2006), shows a well-defined warm core sloping in the direction of vortex tilt. A relative maximum occurs at low-to-mid levels on the south side as a result of subsidence warming, similar to results seen in other simulations of hurricanes in shear (Ritchie and Elsberry 2001, Zhu et al. 2004). Frank and Ritchie (2001) suggested that shear can lead to lateral eddy heat fluxes that weaken the warm core aloft. In the present case, such a diminution of the warm core was minimal below 10 km and was brief and relatively small above 10 km, indicative of the remarkable resiliency of the vortex despite the strong shear and large tilt. Had the shear persisted longer, a more substantial weakening of the warm core probably would have occurred.

The results of the Erin simulation must be viewed with some caution because the degree of asymmetry is somewhat greater than that observed. For example, while the simulation produces a cloud and precipitation free portion of the eyewall during the time of peak shear, observations from TRMM (see Figs. 6 and 7 of Wu et al. 2006) and geostationary satellites do not support such a high degree of asymmetry. Hence, it is likely that the model is producing more shear, and thereby more vortex tilt, than is realistic. However, given that some hurricanes do attain such large degrees of precipitation asymmetry, the results presented here likely have some relevance to those cases.

5. Comparison to Bonnie

In the simulation of Hurricane Bonnie by Braun et al. (2006), the environmental shear was ~10-12 m s^{-1} between 850-200 mb for much of the simulation. While the vertical motion was characterized by a well-developed wavenumber 1 asymmetry, a large fraction of the upward motion occurred in convective updraft towers (Braun 2006) that were associated with eyewall mesovortices. The updrafts formed when the mesovortices moved into the downshear (downtilt)[3] side of the storm and dissipated on the upshear (uptilt) side, thereby contributing to the wavenumber 1 asymmetry. Despite the roughly constant moderate to strong shear, the storm was characterized by relatively weak tilt (<10 km) during its mature stage (see Fig. 11 of Braun et al. 2006).

In the Erin simulation, prior to the onset of significant shear, the eyewall upward motion organization was also dominated by isolated updrafts and eyewall mesovortices. However, as appreciable shear developed (e.g., after 48 h), the vertical motion quickly organized into a prominent wavenumber 1 pattern in which the upward motion occurred within larger, more contiguous areas of ascent (Fig. 7b) on the downtilt side of the eyewall. The shear exceeded 10 m s^{-1} for ~36 h (and peaked at 20 m s^{-1}), during which time the tilt exceeded 10 km and reached a maximum value of ~40 km. The magnitude of the asymmetries in Fig. 6d were more than twice those in the Bonnie simulation (not shown).

---

[3] The shear and the tilt directions were approximately the same.

Figure 10 shows a time series of the different wavenumber components of vertical motion in Hurricane Bonnie similar to that shown in Fig. 1b for Erin. In the case of Bonnie, the dominant contribution was from wavenumbers 4 and higher, indicating the large role of convection. The wavenumber 1 contribution was somewhat larger than the azimuthal mean, but much smaller than that from the highest wavenumbers. With the exception of the large values at 10-11 h when the storm was undergoing some spin-up after initialization of the 2-km grid, the wavenumber 1 component was strongest during the time when the vortex tilt was largest or rapidly realigning (~16-24 h, see Fig. 11 of Braun et al 2006) and decreased somewhat after realignment. In the Erin case (Fig. 1b), the highest wavenumber components dominated during the early stages when the shear was weak (prior to 48 h), but following the onset of strong shear, the wavenumber 1 component increased rapidly and attained a magnitude comparable to the highest wavenumbers. Clearly, the occurrence of much stronger shear and development of larger tilt in the Erin case is a major factor in the differences between the two cases.

Conclusions

The organization of vertical motion in a high-resolution simulation of Hurricane Erin has been analyzed and compared to similar results from a simulation of Hurricane Bonnie by Braun et al. (2006). The results of these simulations, both representing hurricanes of moderate intensity (i.e., categories 2 and 3 on the Saffir-Simpson scale) and large size (radius of maximum winds of about 35-45 km), suggest an organization of eyewall updrafts as depicted in Fig. 11, depending on the strength of the vertical wind shear. In the Bonnie simulation, moderate shear (~10 m s^{-1}) produced a wavenumber 1 asymmetry in the vertical motion with upward motion in the downtilt direction. Superimposed upon this asymmetry was an evolution of eyewall updrafts in which the updrafts were closely linked to the formation and movement of eyewall mesovortices, as depicted in Fig. 11a. The mesovortices moved around the eyewall at a speed somewhat less than that of the maximum tangential winds and as they moved into the downtilt side of the hurricane eyewall, the interaction of the mesovortex circulations with the storm-relative environmental flow led to the formation of updrafts collocated with or slightly trailing the mesovortices. As the mesovortices moved into the uptilt side of the eyewall, the updrafts generally weakened or dissipated.

In the simulation of Erin, similar characteristics were seen, but their evolution depended on the magnitude of the shear and the resultant tilt of the hurricane vortex. In the early parts of the simulation period, the shear was very weak. Eyewall mesovortices were evident on all sides of the eyewall and were frequently associated with convective-scale updrafts. As the shear increased, the updrafts formed preferentially on the downshear side of the eyewall (Fig. 11a). As the shear continued to increase, the tilt of the hurricane vortex increased substantially and led to a transformation of the eyewall structure as depicted in Fig. 11b[4]. During this time, the eyewall was dominated by a cyclonic-anticyclonic vortex couplet, with the cyclonic vortex located in the downtilt-left part of the eyewall. In contrast to the period of weaker shear, in which the flow within the eye was generally weak, during the period of strong shear, the vortex couplet produced a substantial flow across the eye and considerable mixing of eyewall vorticity into the eye. An azimuthally broad area of ascent occurred in the downtilt direction where the low-level inflow associated with the shear converged with the outflow from the eye associated with the vortex couplet. The upward motions were most intense during this time of strong shear and large vortex tilt with the largest updraft velocities concentrated closer to the cyclonic vortex (Fig. 6b).

---

[4] The orientation has been changed to match that for the schematic diagram for the Bonnie case.

As the shear weakened, the vortex tilt also decreased so that the vortex eventually realigned, by which time the vertical motion organization was returning to a pattern similar to that depicted in Fig. 11a.

Both storms were of comparable intensity and size, which likely played a role in their similar organization in the presence of shear. Schubert et al. (1999) and Kossin and Schubert (2001) showed that, depending on the initial characteristics of the annulus of vorticity, the mesovortices may mix into the center and coalesce to form a vortex monopole or they may form a set of long-lived mesovortices whose number may vary (Kossin and Schubert 2001, Montgomery et al. 2002). Kossin and Schubert (2001) found that monopoles are more likely to form from smaller or radially broader initial vorticity annuli, while stable mesovortices are more likely to form from larger and radially thinner vorticity annuli. The relatively large radii of the simulated Bonnie and Erin storms may favor the development of the eyewall mesovortices. An important question for future study is what happens in storms with much smaller radii that may not be capable of supporting eyewall mesovortices or that produce vortex monopoles? Will the upward motion still be organized into localized areas of ascent or will it occur in an azimuthally broader skirt of ascent? Clearly, to generalize the results presented herein or to characterize other forms of updraft organization, a greater diversity of simulations reflecting a greater range of sizes and intensities is needed.

To the extent that the precipitation distribution is determined by the distribution of vertical motion, which itself is related to the dynamics of the eyewall/eye and the interaction with the environmental shear, and that these same processes play some role in intensity change, it is possible that better monitoring of the precipitation intensity and organization may provide hints to present or future changes in storm intensity. Indeed, Kelley et al. (2004, 2005) have shown that deep convective towers observed by TRMM and by coastal radars are often precursors to intensification. Cecil and Zipser (1999) have noted some correlation between ice-scattering signatures from microwave remote sensors and current and future intensity change. These results suggest that utilization of remote sensing of precipitation, combined with increased understanding of the processes relating precipitation organization to the hurricane dynamics and intensity change, could lead to improved monitoring and forecasting of hurricane intensity change.

Acknowledgement: This work was supported by Dr. Ramesh Kakar at NASA Headquarters with funds from the NASA CAMEX-4 and Precipitation Measurement Missions Science programs. The simulations were conducted on NASA Center for Computational Sciences facilities.

References

Bender, M. A., 1997: The effect of relative flow on the asymmetric structure in the interior of hurricanes. *J. Atmos. Sci.*, **54**, 703-724.

Betts, A. K., 1986: A new convective adjustment scheme. Part I: Observational and theoretical basis. *Quart. J. Roy. Meteor. Soc.*, **112**, 677-692.

————, and M. J. Miller, 1986: A new convective adjustment scheme. Part II: Single column tests using GATE wave, BOMEX, ATEC, and artic air-mass data sets. *Quart. J. Roy. Meteor. Soc.*, **112**, 693-709.

———, and ———, 1993: The Betts-Miller scheme. The representation of cumulus convection in numerical models. K. A. Emanuel and D. J. Raymond, Eds., American Meteor. Soc., 246 pp.

Black, M. L., J. F. Gamache, F. D. Marks, Jr., C. E. Samsury, and H. E. Willoughby, 2002: Eastern Pacific Hurricanes Jimena of 1991 and Olivia of 1994: The effect of vertical shear on structure and intensity. *Mon. Wea. Rev.*, **130**, 2291-2312.

———, R. W. Burpee, and F. D. Marks, Jr., 1996: Vertical motion characteristics of tropical cyclones determined with airborne Doppler radial velocities. *J. Atmos. Sci.*, **53**, 1887-1909.

Blackadar, A. K., 1979: High resolution models of the planetary boundary layer. *Advances in Environmental Science and Engineering*, J. Pfafflin and E. Ziegler, Eds., Vol. 1, No. 1, Gordon and Breach, 50-85.

Braun, S. A., 2002: A cloud-resolving simulation of Hurricane Bob (1991): Storm structure and eyewall buoyancy. *Mon. Wea. Rev.*, 130, 1573-1592.

———, 2006: High-Resolution Simulation of Hurricane Bonnie (1998). Part II: Water budget. *J. Atmos. Sci.,* **63**, 43-64.

———, M. T. Montgomery, and Z. Pu, 2006: High-Resolution Simulation of Hurricane Bonnie (1998). Part I: The Organization of Vertical Motion. *J. Atmos. Sci.,* **63**, 19-42.

Cecil, D. J., and E. J. Zipser, 1999: Relationships between tropical cyclone intensity and satellite-based indicators of inner core convection: 85 GHz ice-scattering signature and lightning. *Mon. Wea. Rev.*, **127**, 103-123.

———, and ———, 2002: Reflectivity, ice scattering, and lightning characteristics of hurricane eyewalls and rainbands. Part II: Intercomparison of observations. *Mon. Wea. Rev.*, **130**, 785-801.

———, ———, and S. W. Nesbitt, 2002: Reflectivity, ice scattering, and lightning characteristics of hurricane eyewalls and rainbands. Part I: Quantitative description. *Mon. Wea. Rev.*, **130**, 769-784.

Corbosiero, K. L., and J. Molinari, 2002: The effects of vertical wind shear on the distribution of convection in tropical cyclones. *Mon. Wea. Rev.*, **130**, 2110-2123.

Cram, T. A., J. Persing, M. T. Montgomery, and S. A. Braun, 2006: High-resolution simulation of Hurricane Bonnie (1998). Part III: A lagrangian trajectory view on mixing processes between the eye, eyewall, and environment. *J. Atmos. Sci.,* (submitted).

Dudhia, J, 1989: Numerical study of convection observed during the winter monsoon experiments using a mesoscale two-dimensional model. *J. Atmos. Sci.*, **46**, 3077-3107.

———, 1993: A nonhydrostatic version of the Penn State-NCAR mesoscale model: Validation tests and simulation of an Atlantic Cyclone and cold front. *Mon. Wea. Rev.*, **121**, 1493-1513.

Eastin, M. D., W. M. Gray, and P. G. Black, 2005: Buoyancy of convective vertical motions in the inner core of intense hurricanes. Part I: General statistics. *Mon. Wea. Rev.*, **133**, 188-208.

Frank, W. M., and E. A. Ritchie, 1999: Effects of environmental flow upon tropical cyclone structure. *Mon. Wea. Rev.*, **12**, 2044-2061.

——— and ———, 2001: Effects of vertical wind shear on the intensity and structure of numerically simulated hurricanes. *Mon. Wea. Rev.*, **129**, 2249-2269.

Franklin, J. L., S. J. Lord, S. E. Feuer, and F. D. Marks, Jr., 1993: The kinematic structure of Hurricane Gloria (1985) determined from nested analyses of dropwindsonde and Doppler radar data. *Mon. Wea. Rev.,* **121**, 2433-2451.

Garratt, J. R., 1992: *The Atmospheric Boundary Layer*, Cambridge University Press, 316 pp.

Grell, G. A., J. Dudhia, and D. R. Stauffer, 1995: A description of the fifth-generation Penn State/NCAR Mesoscale Model (MM5). NCAR Technical Note (NCAR/TN-398+STR), 122 pp.

Halverson, J. B., J. Simpson, G. Heymsfield, H. Pierce, T. Hock, and L. Ritchie, 2006: Warm core structure of Hurricane Erin diagnosed from high-altitude dropsondes during CAMEX-4. *J. Atmos. Sci.*, (in press).

Janjic, Z. I., 1994: The step mountain eta coordinate model: Further development of the convection, viscous sublayer, and turbulent closure schemes. *Mon. Wea. Rev.*, **122**, 927-945.

Jones, S. C., 1995: The evolution of vortices in vertical shear: Initially barotropic vortices. *Quart. J. Roy. Meteor. Soc.*, **121**, 821-851.

Jorgensen, D. P., E. J. Zipser, and M. A. LeMone, 1985: Vertical motions in intense hurricanes. *J. Atmos. Sci.*, **42**, 839-856.

Kaplan, J., and M. DeMaria, 2003: Large-scale characteristics of rapidly intensifying tropical cyclones in the North Atlantic basin. *Wea. Forecasting*, **18**, 1093-1108.

Kelley, O. A., J. Stout, and J. B. Halverson, 2004: Tall precipitation cells in tropical cyclone eyewalls are associated with tropical cyclone intensification. *Geophys. Res. Lett.*, **31**, L24112, doi:10.1029/2004GL021616.

———, ———, and ———, 2005: Hurricane intensification detected by continuously monitoring tall precipitation in the eyewall. *Geophys. Res. Lett.*, **32**, L20819,, doi:10.1029/2005GL023583.

Kossin, J. P. and M. D. Eastin, 2001: Two distinct regimes in the kinematic and thermodynamic structure of the hurricane eye and eyewall. *J. Atmos. Sci.*, **58**, 1079-1090.

——— and W. H Schubert, 2001: Mesovortices, polygonal flow patterns, and rapid pressure falls in hurricane-like vortices. *J. Atmos. Sci.,* **58**, 2196-2209.

Lonfat, M., F. D. Marks, Jr., and S. S. Chen, 2004: Precipitation distribution in tropical cyclones using the Tropical Rainfall Measuring Mission (TRMM) microwave imager: A global perspective. *Mon. Wea. Rev.*, **132,** 1645-1660.

Marks, F., Jr., R. A. Houze, Jr., and J. F. Gamache, 1992: Dual-aircraft investigation of the inner core of Hurricane Norbert. Part I: Kinematic structure. *J. Atmos. Sci.*, **49**, 919-942.

McCumber, M., W.-K. Tao, J. Simpson, R. Penc, and S.-T. Soong, 1991: Comparison of ice-phase microphysical parameterization schemes using numerical simulations of tropical convection. *J. Appl. Meteor.*, **30**, 985-1004.

Montgomery, M. T., and L. J. Shapiro, 1995: Generalized Charney-Stern and Fjortoft theorems for rapidly rotating vortices. *J. Atmos. Sci.*, **52**, 1829-1833.

————, V. A. Vladimirov, and P. V. Denissenko, 2002: An experimental study on hurricane mesovortices. *J. Fluid Mech.*, **471**, 1-32.

Nolan, D. S., and M. T. Montgomery, 2002: Nonhydrostatic, three-dimensional perturbations to balanced, hurricane-like vortices. Part I: Linearized formulation, stability, and evolution. *J. Atmos. Sci.*, **59**, 2989-3020.

Pagowski, M., and G. W. K. Moore, 2001: A numerical study of an extreme cold-air outbreak over the Labrador Sea: Sea Ice, air-sea interaction, and development of polar lows. *Mon. Wea. Rev.*, **129**, 47-72.

Persing, J., and M. T. Montgomery 2003: Hurricane superintensity. *J. Atmos. Sci.*, **60**, 2349-2371.

Pu, Z.-X., W.-K. Tao, S. A. Braun, J. Simpson, Y. Jia, J. Halverson, W. Olson, and A. Hou, 2002: The impact of TRMM data on mesoscale numerical simulation of SuperTyphoon Paka. *Mon. Wea. Rev*, **130**, 2448-2458.

Reasor, P. D., and M. T. Montgomery, and L. D. Grasso, 2004: A new look at the problem of tropical cyclones in vertical shear flow: Vortex resiliency. *J. Atmos. Sci.*, **61,** 3-22.

———, ———, F. D. Marks Jr., and J. F. Gamache, 2000: Low-wavenumber structure and evolution of the hurricane inner core observed by airborne dual-Doppler radar. *Mon. wea. Rev.*, **128**, 1653-1680.

Ren, S., 1999: Further results on the stability of rapidly rotating vortices in the asymmetric balance formulation. *J. Atmos. Sci.*, **56**, 475-482.

Riehl, H., and J. S. Malkus, 1961: Some aspects of Hurricane Daisy, 1958. *Tellus*, **13**, 181-213.

Ritchie, E. A., and R. L. Elsberry, 2001: Simulations of the transformation stage of the extratropical transition of tropical cyclones. *Mon. wea. Rev.*, **129**, 1462-1480.

Rogers, R, S. Chen, J. Tenerelli, and H. Willoughby, 2003: A numerical study of the impact of vertical shear on the distribution of rainfall in Hurricane Bonnie (1998), *Mon. Wea. Rev.*, **131**, 1577-1599.

Schubert, W. H., M. T. Montgomery, R. K. Taft, T. A. Guinn, S. R. Fulton, J. P. Kossin, and J. P. Edwards, 1999: Polygonal eyewalls, asymmetric eye contraction, and potential vorticity mixing in hurricanes. *J. Atmos. Sci.*, **56**, 1197-1223.

Shapiro, L. J., 1983: The asymmetric boundary layer flow under a translating hurricane. *J. Atmos. Sci.*, **40**, 1984-1998.

Tao, W.-K., and J. Simpson, 1993: The Goddard Cumulus Ensemble Model. Part I.: Model description. *Terr. Atmos. Oceanic Sci.*, **4**, 35-72.

Wang, Y., and G. J. Holland, 1996: The beta drift of baroclinic vortices. Part I: Adiabatic vortices. *J. Atmos. Sci.*, **53**, 411-427.

Wu, L., S. A. Braun, J. Halverson, and G. Heymsfield, 2006: A numerical study of Hurricane Erin (2001). Part I: Model verification and storm evolution. *J. Atmos. Sci.,* special CAMEX issue (in press).

Zhang, D.-L., and R. A. Anthes, 1982: A high-resolution model of the planetary boundary layer—Sensitivity tests and comparisons with SESAME-79 data. *J. Appl. Meteor.*, **21**, 1594-1609.

Zhu, T., D.-L. Zhang, and F. Weng, 2004: Numerical simulation of hurricane Bonnie (1998). Part I: Eyewall evolution and intensity changes. *Mon. Wea. Rev.*, **132**, 225-241.

FIGURE CAPTIONS

Figure 1. Time series of the amplitude of the (a) tangential velocity near the top of the boundary layer (0.7 km) and (b) vertical velocity at 5.2 km averaged over the radial band between 20 and 70 km. Different lines correspond to the symmetric component (wavenumber 0), wavenumber 1, wavenumber 2, wavenumber 3, and wavenumbers 4 and higher. Labeling on the abscissa shows the forecast hour as well as the time and date (i.e., 00/08 = 00 UTC 8 September).

Figure 2. Map showing the model domains. The outermost two boxes correspond to the 36- and 12-km domains of the simulation by Wu et al. (2006) while the innermost two boxes correspond to the 6- and 2-km grids. The 2-km grid is gradually moved northwestward over the course of the simulation, as indicated.

Figure 3. Time series of simulated (thin line) and observed (thick line) (a) minimum sea-level pressure and (b) maximum wind speed at the lowest model level. The dashed line shows the magnitude of the 850-200 mb vertical wind shear averaged over a radius of 300 km. Labeling on the abscissa shows the forecast hour as well as the time and date (i.e., 00/08 = 00 UTC 8 September).

Figure 4. Simulated precipitation structure at the lowest model level (38 m). Contours show the simulated radar reflectivity averaged over the 6-h period ending at the indicated time. Arrows show the 6-h averaged 850-200 mb vertical wind shear vector. Axis labels are in km with the origin at the storm center.

Figure 5. Simulated vertical motion (shading) at 5.2 km averaged over the 6-h period ending at the indicated time. Areas of significant upward motion are highlighted by contours drawn at 0.5 and 1.5 m s^{-1}. Arrows show the 6-h averaged 850-200 mb vertical wind shear vector. Axis labels are in km with the origin at the storm center.

Figure 6. (a-c) Absolute vorticity (shading), vertical velocity (contours, updrafts only), and storm-relative asymmetric wind vectors averaged over the lowest 3 km at (a) 41 h, (b) 59 h, and (c) 96 h. The contour interval for vorticity is 1×10^{-3} s^{-1} starting at 2×10^{-3} s^{-1}. Contours of vertical motion are at 2 m s^{-1} intervals starting at 2 m s^{-1} with an extra contour at 1 m s^{-1}. Asymmetric wind vectors are obtained by subtracting the azimuthally averaged radial and tangential winds. The vector scale is indicated above the upper-left corner of each panel. (d) Similar to (b), but showing the wavenumbers 1 and 2 vorticity, vertical motion, and asymmetric flow at 59 h. The contour interval is 1 m s^{-1} for vertical velocity and 1×10^{-3} s^{-1} for vorticity. Negative vertical motions are indicated by dashed lines while regions of negative asymmetric vorticity are indicated by the white and stippled regions in (d).

Figure 7. Time-azimuth distributions of radially (16-50 km) and vertically (0-3 km) averaged (a) absolute vorticity, contour interval of 0.5×10^{-3} s^{-1} starting at 1×10^{-3} s^{-1}, and (b) vertical velocity, contours at 0.6 m s^{-1} intervals starting at 0.3 m s^{-1}. The plot has been extended to two revolutions around the center. Labeling on the ordinate shows the forecast hour as well as the corresponding time and date (i.e., 00/08 = 00 UTC 8 September).

Figure 8. Displacement of the storm center at (a) 5.9 km and (b) 9.3 km from the surface center. Time (model hour) is indicated by the asterisks and numbers while the line gets lighter with time.

Figure 9. Vertical cross sections aligned in the direction of vortex tilt at 72 h (00 UTC 10 September) showing simulated radar reflectivity (shading) and (a) tangential velocity, contours at 5 m s^{-1} intervals starting at 15 m s^{-1}, and (b) potential temperature perturbation, contours at 2 K intervals, with negative values indicated by dashed lines and the zero contour by dotted lines. The potential temperature perturbation is obtained by subtracting a reference profile, described in the text, from the full potential temperature.

Figure 10. Time series of the amplitude of the vertical velocity at 5.0 km averaged over the radial band between 30 and 80 km from the simulation of Hurricane Bonnie. Different lines correspond to the symmetric component (wavenumber 0, thick solid line), wavenumber 1 (dashed), wavenumber 2 (dotted), wavenumber 3 (dash-dotted), and wavenumbers 4 and higher (thin solid line). Labeling on the abscissa shows the forecast hour as well as the time and date (i.e., 00/23 = 00 UTC 23 August).

Figure 11. Schematic diagram summarizing (a) the interaction between eyewall mesovortices and the low-level inflow associated with weak-to-moderate environmental wind shear; (b) similar to (a), but for strong shear. The elongated semicircular areas indicate where shear effects favor low-level convergence (light shading) and divergence (cross hatching). The relative flow associated with the environmental shear is indicated by the straight arrows. In (a), the mesovortices and their local cyclonic circulations are indicated by darkly shaded circles and

curved arrows. In (b), a cyclonic/anticyclonic vortex couplet is indicated by the dark/light shaded ovals and their associated circulations by curved arrows. The semitransparent, lightly shaded ovals represent areas of enhanced low-level convergence and upward motion. The orientation of the eyewall asymmetry is held fixed in this figure and may not necessarily match that of the simulations.

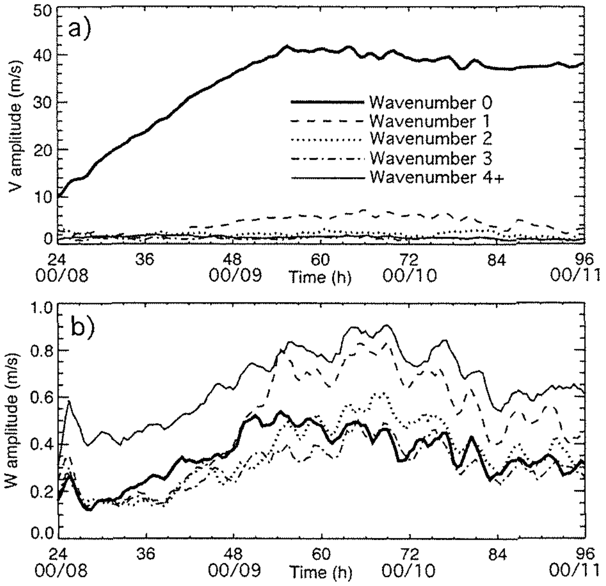

Figure 1. Time series of the amplitude of the (a) tangential velocity near the top of the boundary layer (0.7 km) and (b) vertical velocity at 5.2 km averaged over the radial band between 20 and 70 km. Different lines correspond to the symmetric component (wavenumber 0), wavenumber 1, wavenumber 2, wavenumber 3, and wavenumbers 4 and higher. Labeling on the abscissa shows the forecast hour as well as the time and date (i.e., 00/08 = 00 UTC 8 September).

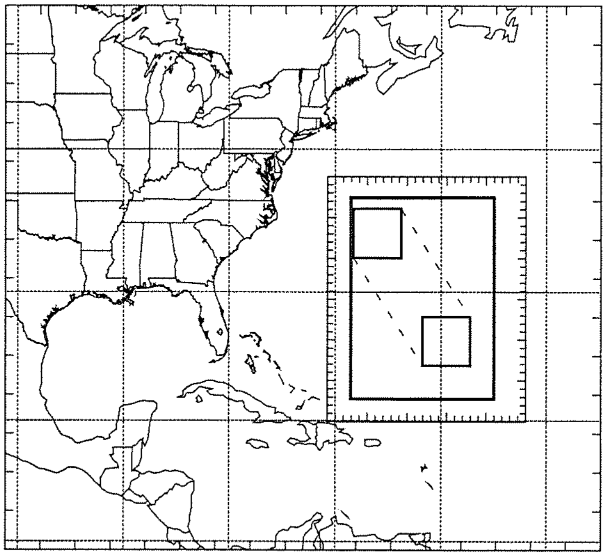

Figure 2. Map showing the model domains. The outermost two boxes correspond to the 36- and 12-km domains of the simulation by Wu et al. (2006) while the innermost two boxes correspond to the 6- and 2-km grids. The 2-km grid is gradually moved northwestward over the course of the simulation, as indicated.

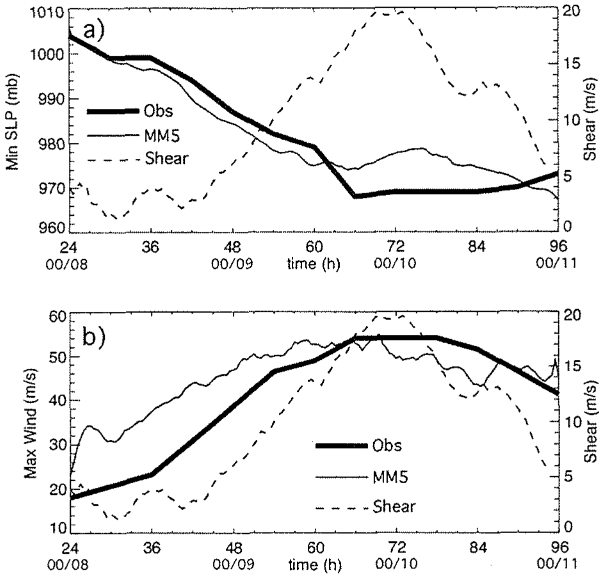

Figure 3. Time series of simulated (thin line) and observed (thick line) (a) minimum sea-level pressure and (b) maximum wind speed at the lowest model level. The dashed line shows the magnitude of the 850-200 mb vertical wind shear averaged over a radius of 300 km. Labeling on the abscissa shows the forecast hour as well as the time and date (i.e., 00/08 = 00 UTC 8 September).

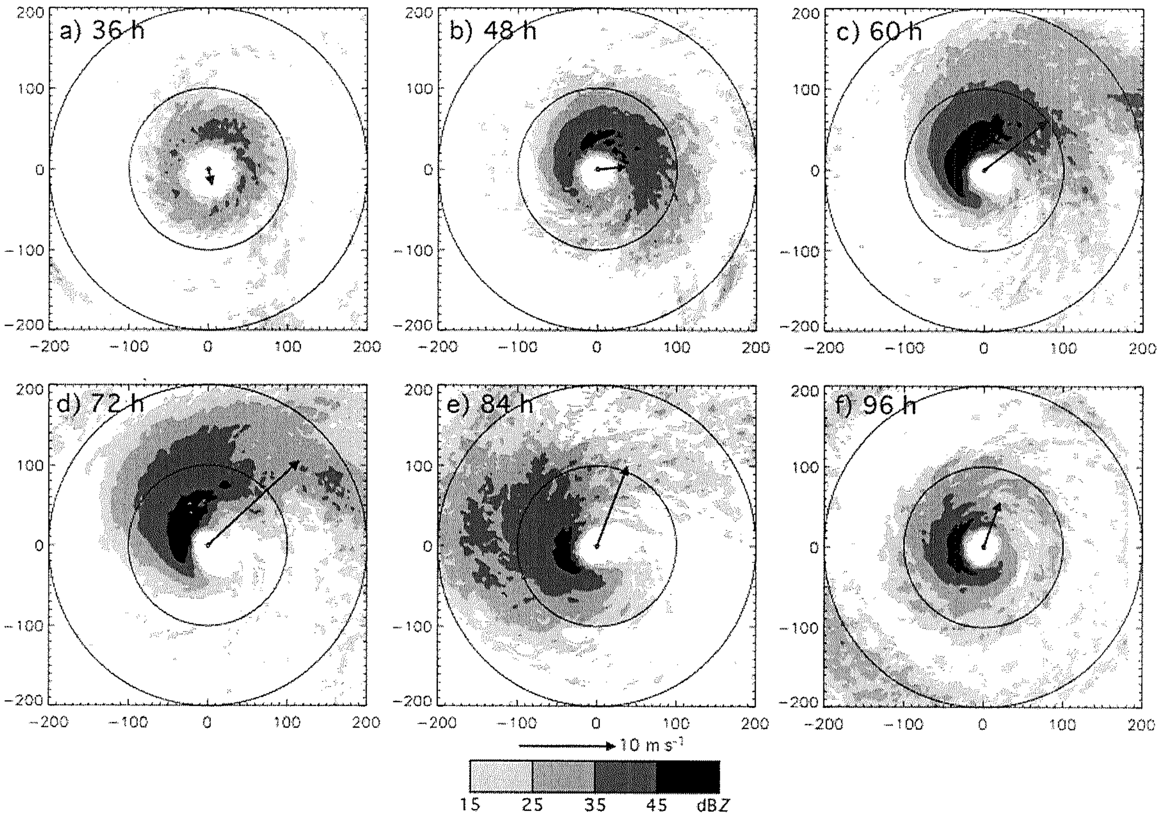

Figure 4. Simulated precipitation structure at the lowest model level (38 m). Contours show the simulated radar reflectivity averaged over the 6-h period ending at the indicated time. Arrows show the 6-h averaged 850-200 mb vertical wind shear vector. Axis labels are in km with the origin at the storm center.

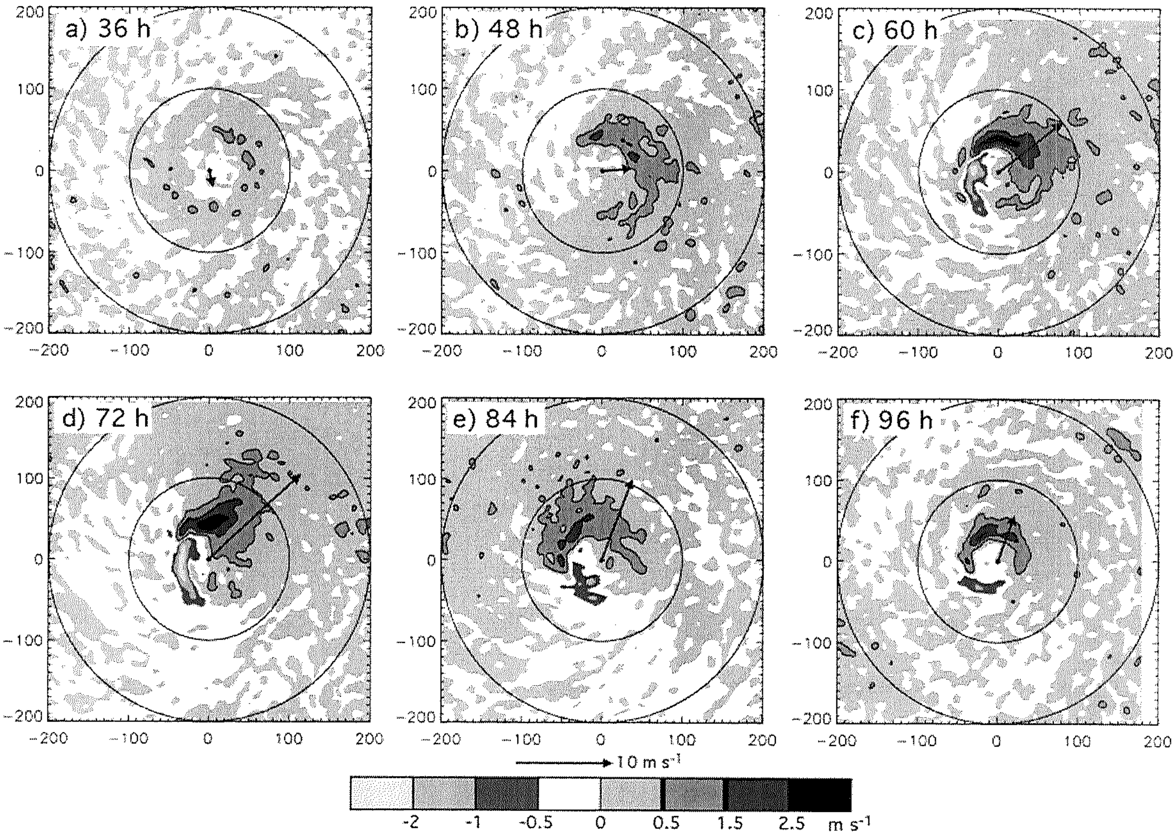

Figure 5. Simulated vertical motion (shading) at 5.2 km averaged over the 6-h period ending at the indicated time. Areas of significant upward motion are highlighted by contours drawn at 0.5 and 1.5 m s^{-1}. Arrows show the 6-h averaged 850-200 mb vertical wind shear vector. Axis labels are in km with the origin at the storm center.

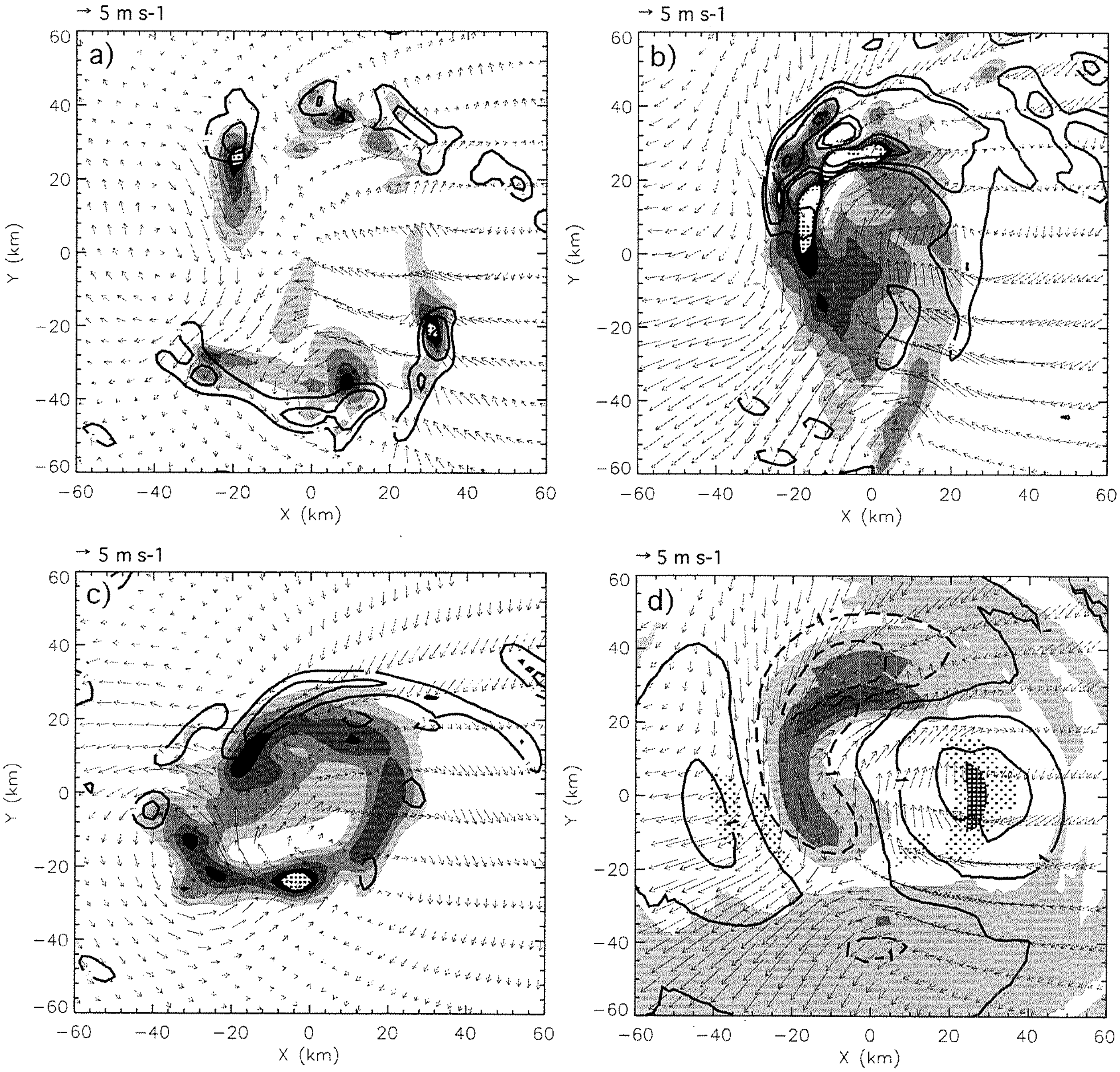

Figure 6. (a-c) Absolute vorticity (shading), vertical velocity (contours, updrafts only), and storm-relative asymmetric wind vectors averaged over the lowest 3 km at (a) 41 h, (b) 59 h, and (c) 96 h. The contour interval for vorticity is 1×10^{-3} s^{-1} starting at 2×10^{-3} s^{-1}. Contours of vertical motion are at 2 m s^{-1} intervals starting at 2 m s^{-1} with an extra contour at 1 m s^{-1}. Asymmetric

wind vectors are obtained by subtracting the azimuthally averaged radial and tangential winds. The vector scale is indicated above the upper-left corner of each panel. (d) Similar to (b), but showing the wavenumbers 1 and 2 vorticity, vertical motion, and asymmetric flow at 59 h. The contour interval is 1 m s^{-1} for vertical velocity and 1×10^{-3} s^{-1} for vorticity. Negative vertical motions are indicated by dashed lines while regions of negative asymmetric vorticity are indicated by the white and stippled regions in (d).

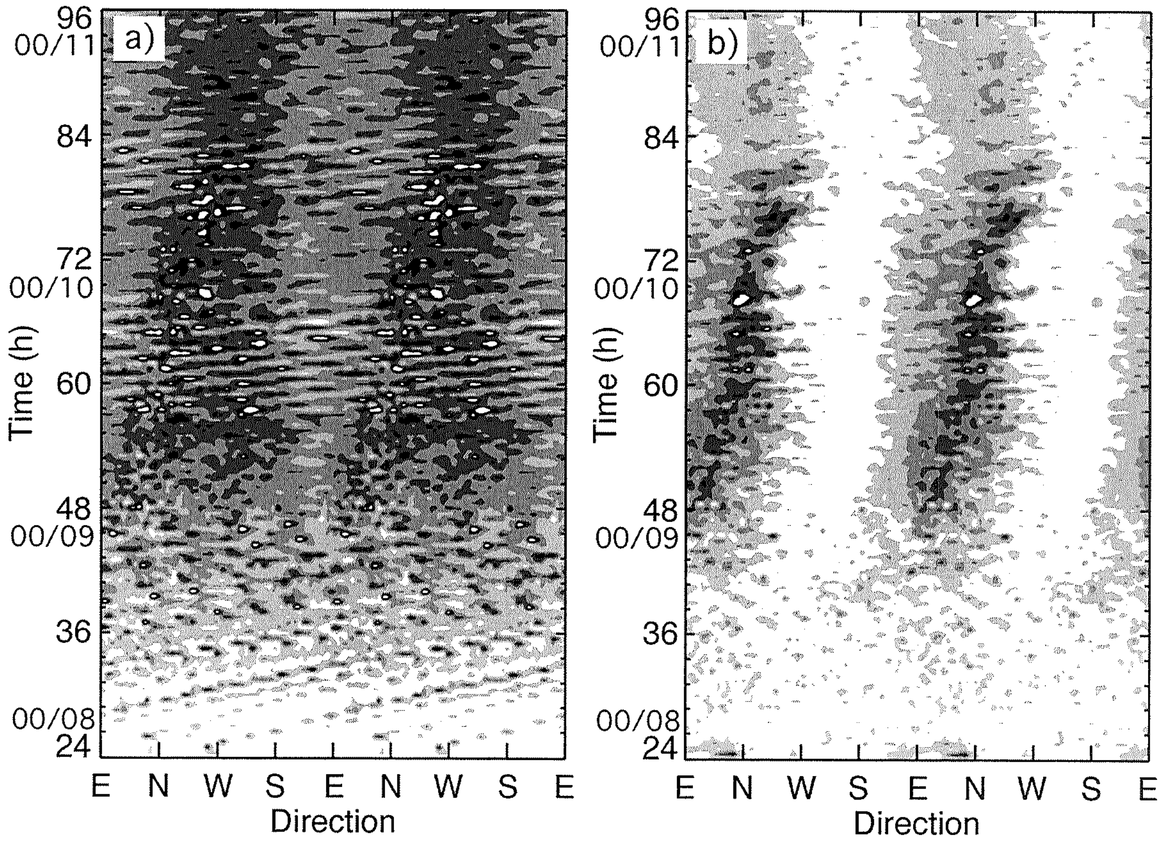

Figure 7. Time-azimuth distributions of radially (16-50 km) and vertically (0-3 km) averaged (a) absolute vorticity, contour interval of 0.5×10^{-3} s^{-1} starting at 1×10^{-3} s^{-1}, and (b) vertical velocity, contours at 0.6 m s^{-1} intervals starting at 0.3 m s^{-1}. The plot has been extended to two revolutions around the center. Labeling on the ordinate shows the forecast hour as well as the corresponding time and date (i.e., 00/08 = 00 UTC 8 September).

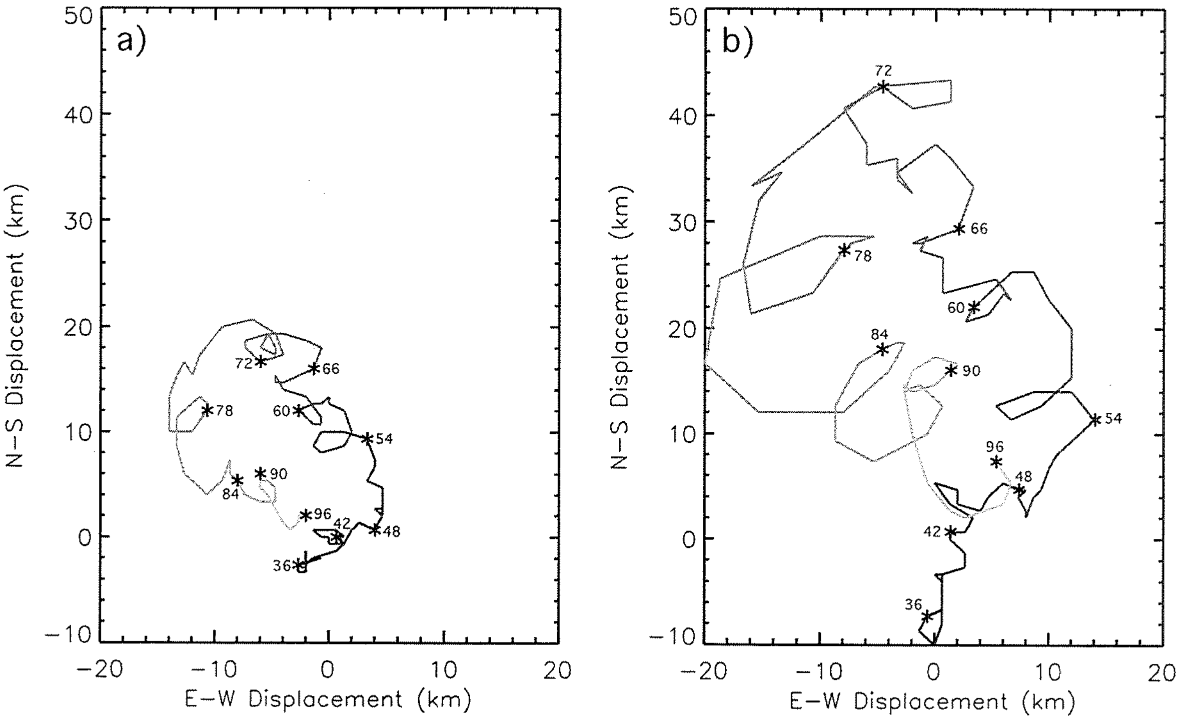

Figure 8. Displacement of the storm center at (a) 5.9 km and (b) 9.3 km from the surface center. Time (model hour) is indicated by the asterisks and numbers while the line gets lighter with time.

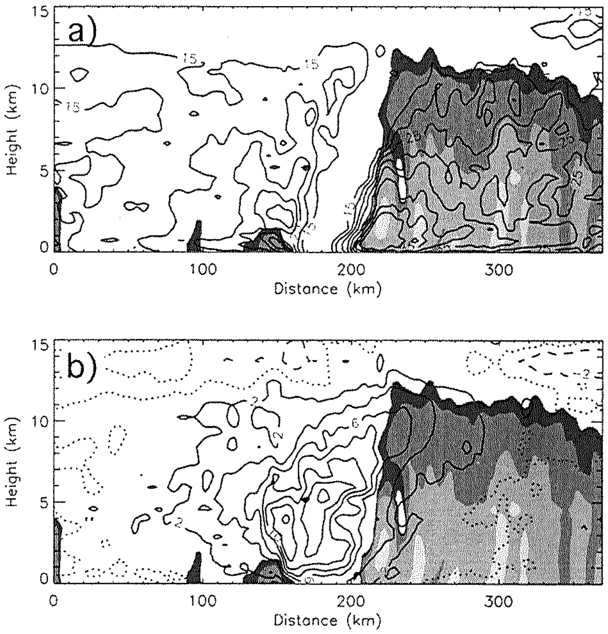

Figure 9. Vertical cross sections aligned in the direction of vortex tilt at 72 h (00 UTC 10 September) showing simulated radar reflectivity (shading) and (a) tangential velocity, contours at 5 m s^{-1} intervals starting at 15 m s^{-1}, and (b) potential temperature perturbation, contours at 2 K intervals, with negative values indicated by dashed lines and the zero contour by dotted lines. The potential temperature perturbation is obtained by subtracting a reference profile, described in the text, from the full potential temperature.

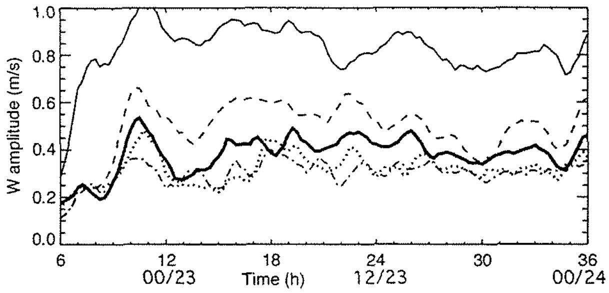

Figure 10. Time series of the amplitude of the vertical velocity at 5.0 km averaged over the radial band between 30 and 80 km from the simulation of Hurricane Bonnie. Different lines correspond to the symmetric component (wavenumber 0, thick solid line), wavenumber 1 (dashed), wavenumber 2 (dotted), wavenumber 3 (dash-dotted), and wavenumbers 4 and higher (thin solid line). Labeling on the abscissa shows the forecast hour as well as the time and date (i.e., 00/23 = 00 UTC 23 August).

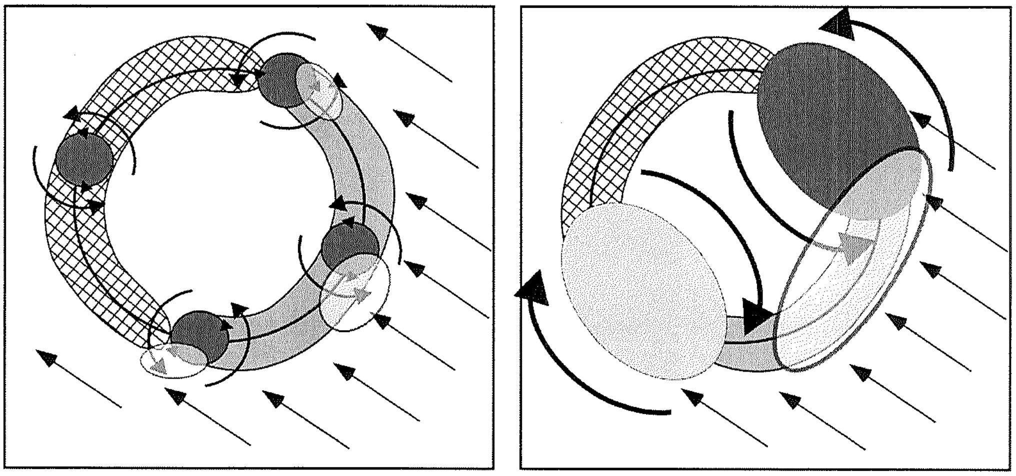

Figure 11. Schematic diagram summarizing (a) the interaction between eyewall mesovortices and the low-level inflow associated with weak-to-moderate environmental wind shear; (b) similar to (a), but for strong shear. The elongated semicircular areas indicate where shear effects favor low-level convergence (light shading) and divergence (cross hatching). The relative flow associated with the environmental shear is indicated by the straight arrows. In (a), the mesovortices and their local cyclonic circulations are indicated by darkly shaded circles and curved arrows. In (b), a cyclonic/anticyclonic vortex couplet is indicated by the dark/light shaded ovals and their associated circulations by curved arrows. The semitransparent, lightly shaded ovals represent areas of enhanced low-level convergence and upward motion. The orientation of the eyewall asymmetry is held fixed in this figure and may not necessarily match that of the simulations.